Estimation of Errors in Stress Distributions Computed in Finite Element Simulations of Polycrystals

Kamalika Chatterjee[1] · Robert A. Carson[1] · Paul R. Dawson[1]

Abstract

The accuracy of the stresses predicted from crystal plasticity-based finite element formulation depends on estimation and control of the errors associated with the discretization. In the current work, the errors in the stress distribution are estimated in virtual polycrystalline samples of α-phase titanium (hexagonal close-packed phase of Ti–6Al–4V). To estimate the error, the stress field, which does not possess inter-element continuity, is smoothed over a grain using an L_2 projection, thereby providing continuous stress distributions with inter-element continuity. The differences between the continuous (smooth) and discontinuous (raw) stress fields are calculated at individual Gauss quadrature points and used to estimate errors for corresponding elements and grains. Error estimations are performed for a Voronoi-tessellated microstructure, an equiaxed microstructure, and two microstructures with varying grain sizes for tensile loading extending into the fully plastic regime ($\approx 5\%$ extension). Magnitudes of the errors are found to depend on microstructural characteristics, particularly the shape and size of grains. Samples having variations in grain size or having less spherical grains exhibited higher errors than samples with uniformly sized, equiaxed grains, with the size variations having a more pronounced effect. Errors correlate with proximity to grain boundaries at small (elastic) strains and with deformation-induced features (deformation bands) at large strains.

Keywords Crystal plasticity · Virtual polycrystals · Stress distributions · Finite elements · Error estimation

Introduction

Finite element simulation at the crystal scale is a frequently used tool for investigating the mechanical properties of structural alloys and minerals. Simulations can be conducted in coordination with experiments to reveal and interpret the physical behaviors of complex polyphase, polycrystalline materials. For crystal-scale simulations, experimental data that are particularly germane derive from characterization methods, such as electron back-scattered diffraction (EBSD), and from mechanical testing, such as high-energy X-ray diffraction (HEXD) or neutron diffraction (ND) with in situ loading. Behaviors that have been studied include yielding,

fatigue and fracture, and the evolution of the state (including texture and strength) [1]. Stress is a critical focus of these efforts, whether directly or indirectly, via its effect on the onset of yielding, the locations of points of failure, or the evolution of state. Assessing the accuracy of the stress predictions is important to assigning confidence to any conclusion drawn from the simulation results.

The finite element method is a general numerical approach for solving boundary value problems. It has its roots in solid mechanics and has become the dominant method for performing stress analyses [2]. While certain practices are now well accepted, there is no universal formulation for all applications. Rather, there are choices exercised in all aspects of the method, including the type of interpolation, the integration rules, and the origin of the residuals, and the linearization technique (for nonlinear systems). These choices exhibit different performance characteristics, which can be exploited according to the attributes of the application to render improved accuracy, speed and robustness. It is not essential that an optimal formulation be identified and used by all. Instead, what is important is that a level of confidence can be assigned to results so that appropriate

✉ Paul R. Dawson
  prd5@cornell.edu

1 Sibley School of Mechanical and Aerospace Engineering, Cornell University, 405 Upson Hall, Ithaca, NY 14850, USA

interpretations are drawn relative to the issues under study. For that, an estimate of the possible error of a simulation is needed. In assessing the error associated with a simulation, it is useful to draw a distinction between error that might be introduced by equations that represent the mechanical behavior (the model) and error that arises because the method to solve the model equations (the solver) might not have delivered the exact answer. This distinction is referred to as validation versus verification [3, 4]. Validation and verification of the simulation models both are essential for building confidence in the simulation results.

In modeling the elastoplastic behavior of polycrystals, numerous choices must be made in defining and executing simulations. To begin, a specific polycrystalline virtual sample must be instantiated. This involves laying out the spatial arrangement of the individual grains, assigning attributes to the grains (such as phase, lattice orientation and strength), and creating an appropriate mesh. Given a complete virtual sample, the simulation can be executed for prescribed initial and boundary conditions using a formulation that embodies constitutive models and attendant numerical methods that are appropriately chosen to render an accurate solution. Validation involves the critical assessment that the virtual sample and the equations that govern its response are capable of accurately representing a polycrystal's mechanical behavior. Validation has been the focus of prior publications for crystal-scale simulations, for example in [5, 6]. Using a more formal uncertainty quantification framework, Rizzi et al. [7] examined predictions for continuum, isotropic plasticity formulation for an additive manufacturing application.

Here the focus is on verification. In particular, is the mesh of the instantiated sample adequate? This question is addressed by examining estimates of the spatial distribution of error in the stress prediction. The methodology applied to estimate error has been used in the past for adaptive meshing [8]. An existing finite element code (*FEpX*) for crystal-scale simulations is employed here to examine error in the stress distributions [9]. The formulation has been used previously to investigate the responses of a variety of metals, including titanium alloys [10–12] (for convenience, a summary of the crystal-scale elastoplastic model and its finite element implementation are provided in the supplement entitled, "Finite Element Methodology Supplement", in addition to the reference cited above). Methods of the instantiation of the virtual polycrystal are considered, however, with attention to how attributes of the instantiation influence the distributions of error.

The paper is arranged in the following format. First the methodology to estimate error of the stress distribution is reviewed. Next, the instantiation of virtual samples with different types of microstructures is presented, which is followed with a summary of information related to the simulations (namely, critical 'input' and 'output' data). The results

are presented in several sections dedicated to particular issues: convergence of the solution with mesh resolution; sensitivity of the error to the type of microstructure; the influence of the grain boundary representation on error; the correlation of intragrain lattice misorientation to error. The body of the paper finishes with a set of conclusions.

Error Estimation Methodology

One approach to obtaining accurate, converged solutions in finite element analyses is to control the magnitude of the potential error through refinement or coarsening of the spatial discretization (typically, the mesh resolution) [2]. In this case, the error is defined as the difference between the finite element solution and the exact solution. To determine an adequate level of mesh refinement, one needs to estimate the error that can be attributed to the discretization. However, the exact solution typically is not available in advance, and so one must adopt a method to estimate error without knowing the exact solution. Fortunately, an estimate of the error can be computed using information available from the finite element solution itself. Field data available from finite element simulations, such as the stress and strain, often are processed subsequent to a simulation to improve their accuracy—a process referred to as recovery. Error estimation can employ recovered data as a substitute for the exact solution and thereby provide a posteriori estimates of the error. A posteriori approaches have been explored in depth, as reported by Zienkiewicz et al. [2], Ainsworth et al. [13], Becker and Rannacher [14], and Grätsch and Bathe [15].

An intuitive and effective example of the recovery-based a posteriori error estimation was proposed by Zienkiewicz and Zhu [8]. This method involves comparing the (unprocessed) finite element stresses to a continuous stress field generated by a recovery process. The justification for why this difference is a measure of error stems from the property of a converged solution that the stress field is continuous over regions in which the material properties are continuous. Continuity is a necessary, but not sufficient, condition for the solution to satisfy equilibrium on domains where the properties do not exhibit discontinuities. Thus, within grains of a polycrystal where the properties are continuous, continuity of the stress is expected in a converged solution even though it is not explicitly dictated through the properties of an interpolation function. Conversely, if the stress distribution is not continuous over the domain of a crystal, then the solution is not yet converged. The extent to which it deviates from a continuous solution is a quantification of the error. Note that the objective in refining the discretization is to manage the error, not to eliminate it. Controlling the error refers to reaching a level of refinement that guarantees that the error is below

a specified tolerance everywhere. Ideally, the error is uniform over the discretization, indicating that the refinement is optimally deployed.

Recall that for finite element simulations the unprocessed (raw) stress field is an output of a simulation and is known within elements of the mesh, typically at the quadrature points. With commonly used C^0 elements, the motion is continuous over the entire body (both within and across elements). Derivative kinematic quantities are continuous within elements, but discontinuous between elements. For linear elastic behavior, the same continuity conditions exist for stress that exist for the strain. For nonlinear elastoplastic behaviors, on the other hand, the stress representation is a point-wise evaluation from the constitutive equations to which no functional form is prescribed a priori. The finite element formulation determines the solution that best satisfies equilibrium in a weak sense, but without the precise functional form of the stress distribution ever being explicitly defined. Thus, a stress field that is continuous over appropriate domains, in this case the individual grains of the polycrystal, is not immediately available from the raw finite element stresses. Rather, a continuous stress distribution with inter-element continuity must be created from the point-wise values of stress.

A continuous stress field may be generated in a number of ways: local averaging at nodes, patches, meshless interpolation, and global projection. Here, we employ a hybrid of these, using a projection (known as an L_2 projection) separately over individual grains. The grains of the polycrystal are treated independently as there is no intent to require stress continuity across grain boundaries. For equilibrium, the traction vectors acting on the grain surfaces must be continuous across the surface, but this does not extend to the full stress tensor. With distinct lattice orientations on opposing sides of a grain boundary, there will in general be differences in some stress components in the opposing grains. Thus, we seek a solution with stress continuity only within grains and assume that the lattice orientations within grains are themselves uniform or at least smoothly varying.

With this strategy, a continuous stress distribution over a grain is defined using piecewise-continuous distributions—namely, C^0 finite element interpolation functions. The stress has six independent components, which dictates that there are six stress degrees of freedom at each nodal point of the mesh over a grain. Each degree of freedom of the stress, indicated by the superscript, i, is represented with the finite element interpolation $\sigma^i(\boldsymbol{x}) = [N(\boldsymbol{x})]\{S^i\}$, where $[N(\boldsymbol{x})]$ are the interpolation functions and $\{S^i\}$ are nodal values for component, i. With this representation, the stress is guaranteed to be a continuous function over a grain.

Nodal point values of the stress are determined from quadrature point values within elements via a weighted residual. For each degree of freedom, a weighted residual, R^i, is formed over the volume of a grain, V^{g}, to determine the nodal point values of the stress as prescribed in Eq. 5:

$$R^i = \int_{V^{\mathrm{g}}} \Psi(\boldsymbol{x}) \left[\sigma^i(\boldsymbol{x}) - [N(\boldsymbol{x})]\{S^i\} \right] \mathrm{d}V \tag{1}$$

where $\Psi(\boldsymbol{x})$ is the weighting function. Standard finite element procedures are followed to develop a matrix equation for the nodal point stresses from Eq. 1:

$$[A]\{S^i\} = \{B\} \tag{2}$$

where the elemental contributions for $[A]$ and $\{B\}$, respectively, are:

$$\left[A^{\mathrm{e}} \right] = \int_{V^{\mathrm{e}}} [N(\boldsymbol{x})]^{\mathrm{T}} [N(\boldsymbol{x})] \mathrm{d}V \tag{3}$$

and

$$\{B^{\mathrm{e}}\} = \int_{V^{\mathrm{e}}} [N(\boldsymbol{x})]^{\mathrm{T}} \sigma^i(\boldsymbol{x}) \mathrm{d}V \tag{4}$$

The quadrature point values enter the residual through the field, $\sigma^i(\boldsymbol{x})$, when the right-hand side integral is evaluated by numerical quadrature (thereby utilizing the quadrature point values of the raw stress distribution). The solution of this equation gives the nodal values that provide an optimal fit to the spatial distribution embodied in the raw (quadrature point) stress values.

With the nodal point values of the stress determined, the continuous stress field is known and the error can be evaluated. To do this, all components are concatenated into a single expression, written in Voigt notation as a six vector, $\{\sigma(\boldsymbol{x})\}$:

$$\{\sigma(\boldsymbol{x})\} = [\tilde{N}(\boldsymbol{x})]\{\tilde{S}\} \tag{5}$$

where the tilde symbol indicates concatenations of the respective quantities. The differences between the continuous and discontinuous stress fields, calculated at individual Gauss points, are utilized to estimate the norm of errors element by element:

$$E^{\mathrm{e}} = \frac{\int_{V^{\mathrm{e}}} ||\{\sigma(\boldsymbol{x})\} - [\tilde{N}(\boldsymbol{x})]\{\tilde{S}\}|| \, \mathrm{d}V}{\Sigma V^{\mathrm{e}}} \tag{6}$$

Here, Σ, the nominal stress applied to the polycrystal, is employed to normalize the local stress difference. The normalized errors for individual elements are averaged over the grain to define the grain-averaged error distribution:

$$E^{\mathrm{g}} = \sum_{i=1}^{n^{\mathrm{e}}} E^{\mathrm{e}} \tag{7}$$

Fig. 1 Sample instantiations with: **a** Voronoi tessellation having random grain sizes and shapes; **b** equiaxed tessellation having uniform grain size; **c** bimodal tessellation having two distinct grain sizes; and **d** grain growth tessellation having a distribution of larger grains surrounded by smaller grains

(a)   (b)   (c)   (d)
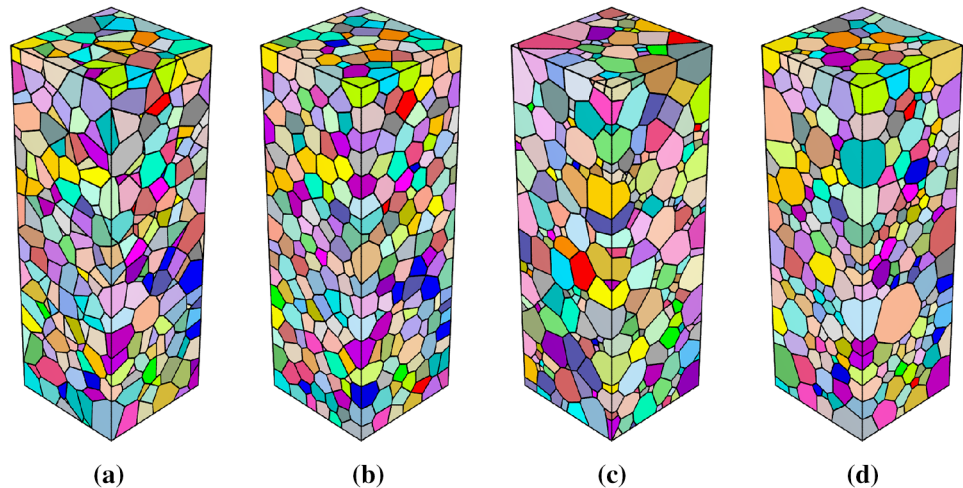
where n^e is the total number of finite elements that belong to a particular grain. The error values can be estimated at each load step of a deformation history to assess the evolving level of error in a simulation.

Virtual Samples: Instantiation and Loading

The investigation reported here examined several aspects of polycrystalline samples: grain size and shape distributions, initial texture, and grain boundary representation. The objective is to explore how the error distributions might be affected by attributes of the microstructure. The variations of attributes are not exhaustive, but rather are intended to demonstrate the potential for sensitivity of the simulation errors to features that are commonly incorporated in sample instantiations. No attempt has been made to include, for example, dislocation structure or second phase particles. In the current work, the errors in the stress distribution are estimated in virtual polycrystalline samples of α-titanium [the hexagonal close-packed (hcp) phase of Ti–6Al–4V]. Ti–6Al–4V is an alloy that displays a rich variety of microstructural features in differing forms depending on how the alloy has been processed [16]. In this section, specifics of the simulations are presented. Simulation inputs are provided specifically for the instantiation of the sample grain structure, the single-crystal mechanical properties, and the simulation boundary conditions.

Grain Structures

Four different types of virtual microstructures were created using Neper [17] and are displayed in Fig. 1. Each type of microstructure has 1000 grains but different characteristics of grain size and shape. The instantiated samples have a 3:1 ratio in length to width, with the length being 1.2 mm and cross section being 0.4 mm × 0.4 mm.

The absolute dimensions do not affect the results as the equations for slip to not have an embedded length scale. The dimensions were arbitrarily chosen with the intent of having realistic grain sizes. Factors that do affect the results, however, are the distribution of grain sizes (discussed in "Influence of Grain Geometry" section) and the numbers of grains on a load-bearing cross section.

The baseline type is a regular Voronoi tessellation that exhibits a random grain size and shape distribution (Fig. 1a). In addition to the sample shown, three equivalent Voronoi samples are generated by changing the location of seed points used for the tessellation. Simulations performed with these samples established that the error distributions do not differ significantly across a set of equivalent samples.

The three other microstructures offer variations from the baseline commonly observed in real microstructures. The first of these is a microstructure (Fig. 1b) with nearly spherical grains of almost equal size. It was created using a Laguerre tessellation and is called an equiaxed microstructure. The two remaining microstructures highlight possible variations in grain size. One of these exhibits a combination of two grain sizes and is referred to here as the bimodal microstructure (Fig. 1c). The other was generated using the grain growth tessellation feature in Neper (Fig. 1d). This microstructure exhibits a large variation of grain size with the grains being nearly spherical in shape.

Frequency distributions for the relative grain size (diameter) and for the grain shape (sphericity) are given in Fig. 2 for the four types of microstructures. Grain size is estimated as the equivalent grain diameter normalized against the average diameter of all the grains, and sphericity is the ratio of the grain volume to the volume of sphere of equal diameter. All of the microstructures possess the same average grain diameter owing to all having the same number of grains and
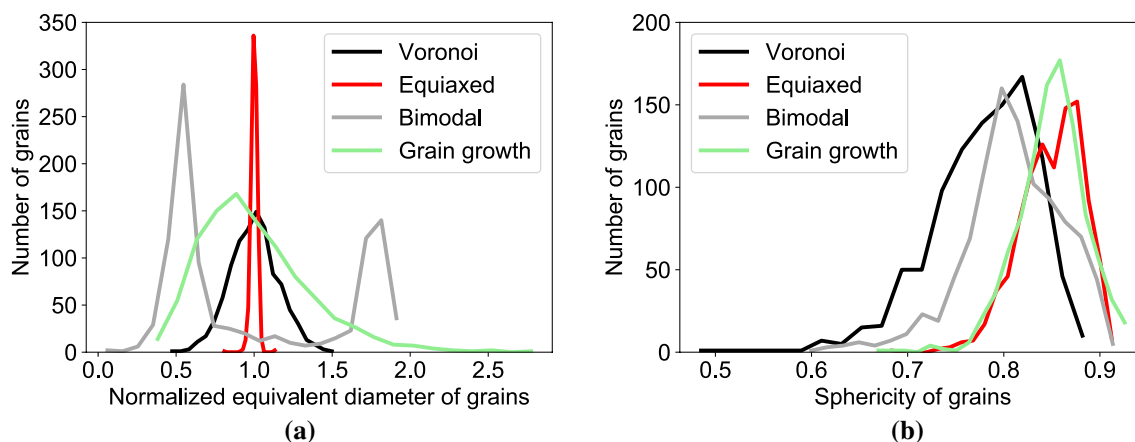
Fig. 2 Sample metrics: **a** relative grain size and **b** sphericity (shape) distributions for the four types of instantiations shown in Fig. 1

the same total volume. The variations in grain size differ markedly, ranging from the very tight distribution of the equiaxed microstructure to the comparatively large spread in sizes within the grain growth microstructure. The two peaks of the bimodal microstructure distribution have similar spreads to the Voronoi microstructure. The sphericity distributions of all the microstructures are qualitatively similar. The Voronoi microstructure shows greater spread in values than the equiaxed, consistent with the attributes of Voronoi and Laguerre tessellations.

Initial Textures

Two initial textures were considered in conjunction with each of the four types of microstructures. Texture here refers to the orientation distribution of the crystallographic lattice. The two textures are displayed in Fig. 3 as inverse poles showing the loading axis with respect to the crystal frame. The first texture (Fig. 3a) is drawn from a uniform distribution. The second texture has two primary components in which 500 grains are oriented with their hcp c-axes closely aligned with the loading direction and 500 grains are oriented with their c-axes at 40°–50° from the loading direction. This is referred to here as the dual texture. In the dual texture sample, the two texture components are distributed randomly over the geometry. For the set of slip parameters used in the current work (see "Results" section), the directional strength-to-stiffness ratio is highest for c-axis being aligned with the loading direction [11]. The directional strength-to-stiffness ratio is computed from the stress need to initiate yielding (strength) and the directional Young's modulus (stiffness). Grains having their c-axis aligned with the loading direction tend to yield and exhibit plastic deformation after grains with other lattice orientations. In contrast, the directional strength-to-stiffness ratio is the lowest for grains oriented at 40°–50°, and slip tends to initiate earlier

in these grains than in grains with other lattice orientations. As a consequence, samples with a combination of these two types of orientations develop strong orientation gradients after plastic deformation and therefore are anticipated to develop higher errors. These two textures were chosen primarily to give contrasting responses—the uniform texture promoting more uniform deformation response and the dual texture promoting strain localization. The baseline texture for the simulations is the dual texture.

Grain Boundary Representation

The four types of microstructure presented in "Grain Structures" section have smooth grain boundaries and are collectively referred to as the 'Smooth GB' samples. A different approach to sample instantiation is to build samples directly from voxel data sets. The final virtual sample may mimic the experimental data and exhibit serrated grain boundaries. To consider simulation errors in this type of sample, samples with serrated grain boundary features were created for the equiaxed and bimodal types of microstructure using a rasterized tessellation. These two types of microstructure were chosen because the error distributions obtained with these two types for the Smooth GB instantiations were the most dissimilar among all the microstructures. The samples
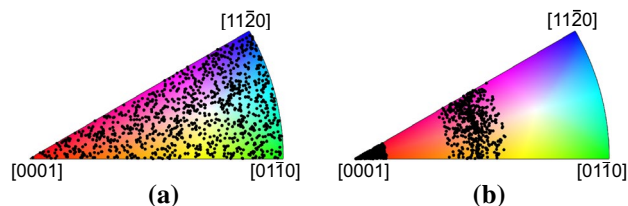

Fig. 3 Two types of initial texture used in the simulations: **a** uniform texture and **b** dual texture
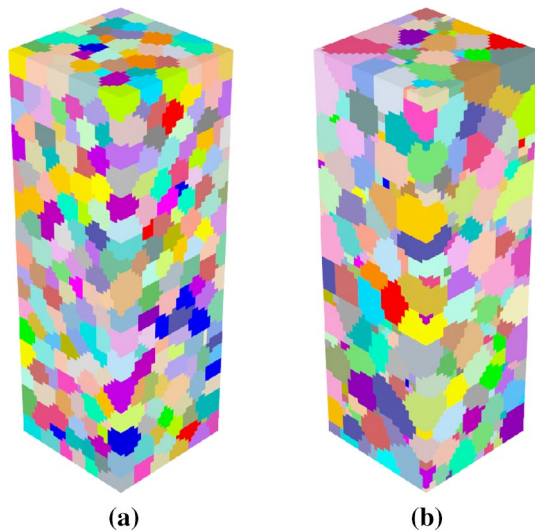
Fig. 4 Virtual microstructures of **a** equiaxed and **b** bimodal grain size distributions with serrated grain boundaries (rasterized tessellations)

Table 1 Single-crystal elastic constants for the α phase of Ti–6Al–4V (see [9] for variable definitions)

C_{11} (GPa)	C_{12} (GPa)	C_{13} (GPa)	C_{44} (GPa)
169.7	88.7	61.7	42.5

Table 2 Initial slip system strengths for the α phase of Ti–6Al–4V, including relative ratios normalized by each set's basal strength. $g_{0,b}$, $g_{0,p}$ and $g_{0,\pi}$ are the initial slip system strengths of the basal, prismatic and pyramidal slip systems, respectively (see [9] for variable definitions)

$g_{0,b}$ (MPa)	$g_{0,p}$ (MPa)	$g_{0,\pi}$ (MPa)	$\frac{g_{0,p}}{g_{0,b}} : \frac{g_{0,\pi}}{g_{0,b}}$
390	468	663	1.2:1.7

Table 3 Voce hardening model parameters used for the α phase of Ti–6Al–4V (see [9] for variable definitions)

h_0 (MPa)	g_{s0} (MPa)	m	m'	$\dot{\gamma}_0$ (s^{-1})	$\dot{\gamma}_{s0}$ (s^{-1})
190	530	0.01	0.01	1.0	5×10^{10}

with serrated boundaries are designated as the 'Serrated GB' samples and are shown in Fig. 4. The final virtual samples thus mimic the experimental data in that they exhibit serrated boundaries that accompany voxel data. Note that these samples have the same number of grains and use the same grain centroid locations as their Smooth GB counterparts in Fig. 1. The Serrated GB samples use only the baseline (dual) texture.

Single-crystal properties

The single-crystal mechanical properties used in simulations control the stress distributions computed. In this investigation, the single-crystal properties of a titanium alloy (Ti–6Al–4V) were selected because of the extensive effort previously invested to quantify the values and the continuing interest in the error estimates associated with simulations conducted for this material. As a simplifying assumption, only the hcp (α) phase is considered. The α-phase volume fraction is approximately 93% of the total for Ti–6Al–4V, but for the virtual samples it constitutes the entire volume. Single-crystal elastic constants are listed in Table 1; values used for the initial slip system strengths are listed in Table 2. The values given in Tables 1 and 2 are determined using HEXD data, with documentation provided in [18, 19], respectively. Although Ti–6Al–4V exhibits little strain hardening, it was included in the simulations. Values for the Voce-type slip system strength evolution equation, listed in Table 3, were defined to match macroscopic stress–strain test data [19]. Simulations performed previously based on characterization of the α-phase have shown good agreement for stress distributions and yield initiation with high-energy X-ray diffraction (HEXD) and digital image correlation (DIC) data [11].

Sample loading

The virtual samples were loaded in uniaxial tension parallel to their long dimension (z-direction in the simulations). The samples were extended to ≈ 5% strain, which is sufficient to cause significant plastic deformation (the initial yield is below 1% strain). The loading was performed in displacement control. In particular, one end of the sample (the bottom surface in the plots) was held fixed, while the other end (the top surface in the plots) was displaced to extend the length of the sample. A velocity was specified to provide a nominal strain rate over the sample of approximately 10^{-3} s^{-1}.

Results

Simulation data were saved throughout the loading sequence. The stored records included the stresses at individual quadrature points, as well as plastic strains, slip system strengths and lattice orientations. Using the methodology presented in "Error Estimation Methodology" section, smooth stress distributions were computed grain-by-grain over entire samples and errors were estimated from the differences between the smoothed and raw stresses. Using this approach, the stress field for each grain is treated independently of the fields in all other grains. This allows for stress discontinuities at
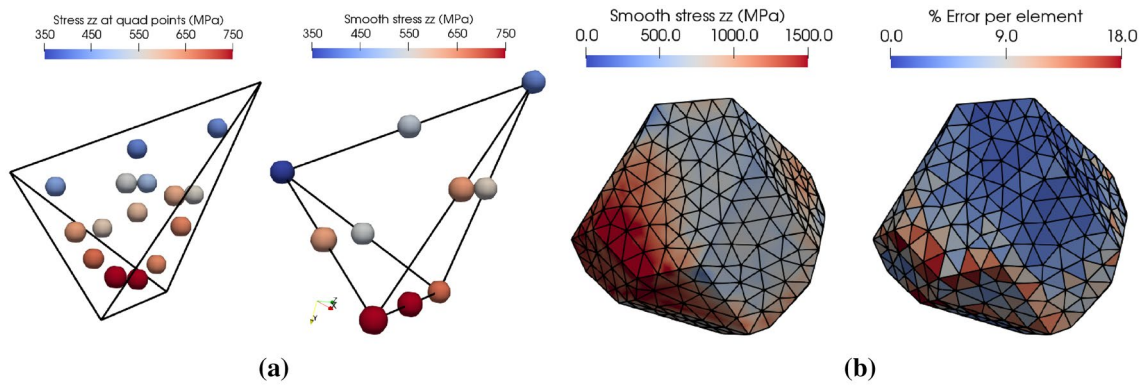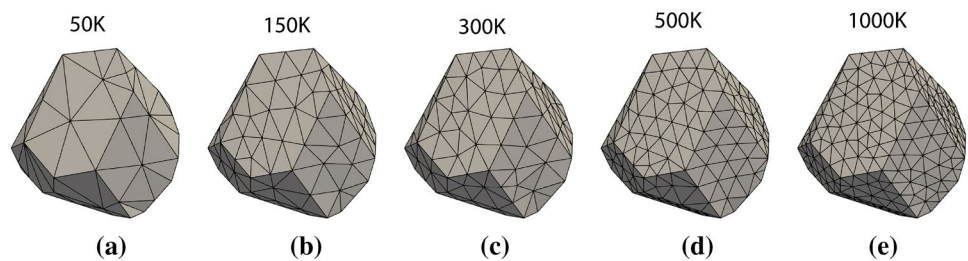
Fig. 5 **a** Quadrature point values of one stress component and corresponding smooth stress distribution (nodal stress values); **b** smooth stress distribution over a single grain and corresponding elemental errors

Fig. 6 Mesh refinement shown in a single grain in the Voronoi tessellation for total mesh size of: **a** 50K, **b** 150K, **c** 300K, **d** 500K and **e** 1000K

the grain boundaries, but enforces continuity within grains. Figure 5 illustrates this process for one stress component. Figure 5a shows the quadrature point (raw) stress values and the corresponding smooth stress distribution over a single element (stress values projected at the nodes). Figure 5b shows the smoothed stress distribution over an entire grain and the elemental errors, computed with Eq. 6 over the same grain, respectively. From the elemental errors, grain-averaged errors were computed and used to compute error distributions over the samples for the full loading histories.

The following subsections present results of all the simulations performed. For the baseline case (Voronoi tessellation and dual texture), we first summarize the results of a mesh refinement study. This study provides insight into the mesh dependence of the stress distributions. Focusing on two levels of refinement, error distributions are discussed in the context of the grain size and shape distributions, the strength of the initial texture, and the grain boundary representation.

Influence of Mesh Refinement

A necessary condition for the guarantee of accurate stress predictions is that the solution converges with increased mesh refinement. For this reason, the error distributions associated with the level of discretization are examined first. The Voronoi-tessellated sample with the dual texture, which

serves as the baseline case, was discretized into 10-node tetrahedral elements using five levels of refinement: 50K, 150K, 300K, 500K and 1000K elements. Figure 6 depicts the finite elements within one of the grains of the sample. The factor of 20 refinement from the 50K element mesh to the 1000K element mesh increases the element density in each spatial direction approximately by a factor of between two and three. Simulations were performed at each level of refinement, and the results were used to quantify the reduction in the stress distribution errors with mesh refinement. Trends with respect to mesh refinement for the baseline case appear in Fig. 7. The macroscopic stress–strain responses (Fig. 7a) are insensitive to the level of mesh refinement. The nominal stress is slightly lower with increasing numbers of elements, as expected. Generally speaking, as the number of degrees of freedom goes up in the case of a refined mesh, the mesh is better able to match the exact motion and the computed driving force for deformation is lower. However, the difference is slight, and consequently, the normalization of the error values with nominal stresses is not biased due to refinement.

Frequency distributions for the average grain error, E^g, are shown in Fig. 7b for all levels of discretization at the end of the loading ($\approx 5\%$ strain). Approximately 500 grains from the central half of the sample (0.6 mm around the center) were considered for plotting this frequency distribution, to avoid the effects of top of bottom boundaries
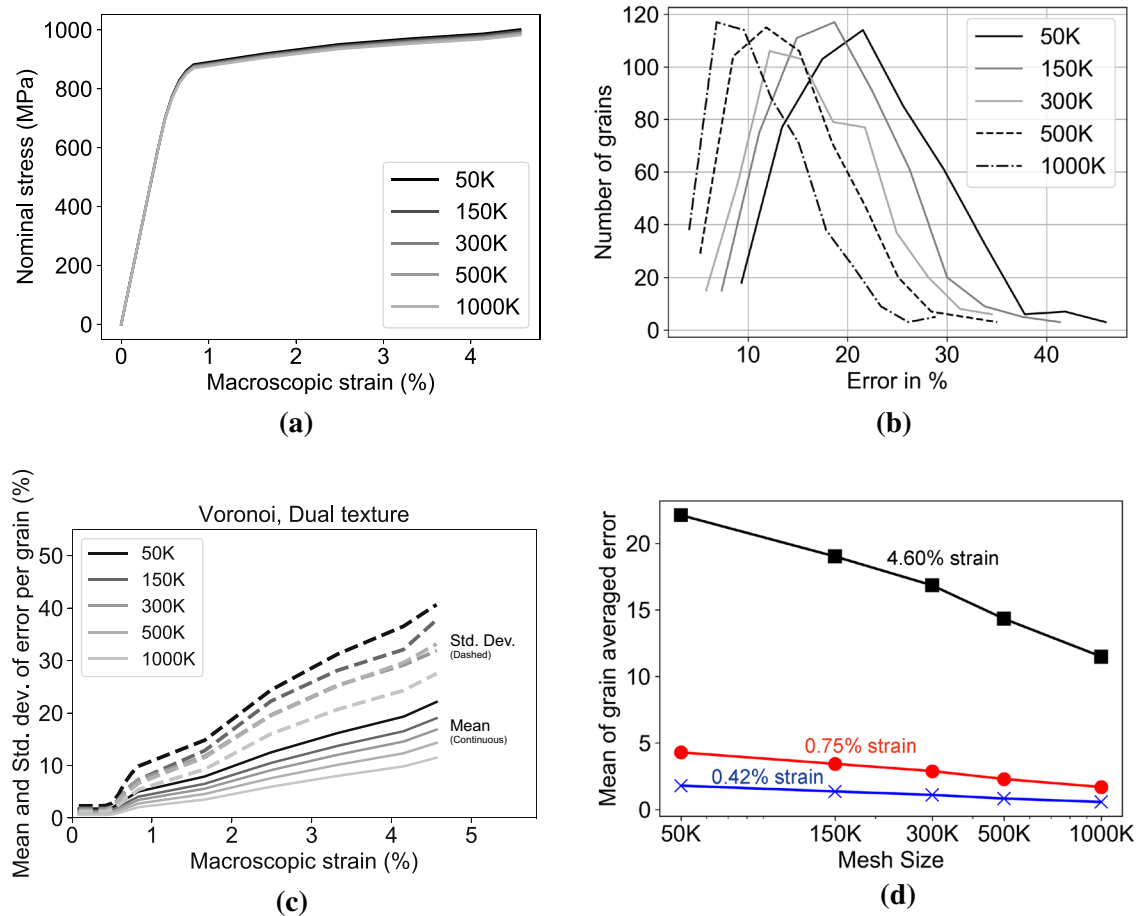
Fig. 7 **a** The macroscopic stress–strain curves for five levels of discretizations (50K, 150K, 300K, 500K and 1000K) for the baseline case (Voronoi tessellation and dual texture). **b** Grain-averaged error distributions for five levels of mesh refinement shown in Fig. 6 at 4.6% strain. **c** Evolution of mean and standard deviation of grain-level error, E^g, with applied strain. **d** Stress convergence with mesh refinement at 0.42%, 0.75% and 4.60% macroscopic strain

where boundary conditions are applied. Some of these grains touch the four free side surfaces of the geometry. The frequency distributions all have similar form, but there is a shift toward lower errors with increased mesh refinement. Mean and standard deviation values for error distributions were computed using grain-averaged error values for grains in the central half of the geometry—the grains within 25% volume from the top and bottom surfaces were not considered for this calculation. The mean and standard deviation values are plotted as a function of sample strain for each level of refinement in Fig. 7c. The mean and standard deviation values overall increase with strain for all levels of refinement. Crucially, there is a consistent trend toward lower values of each metric with higher refinement, indicating convergence of the solution. A maximum grain-level mean error of 20% was observed for the coarsest discretization of 50K elements. With refinement of the mesh, the grain-by-grain error values reduce by nearly a factor of two, as is evident from Fig. 7c.

Overall, the convergence behavior shown in Fig. 7d is typical of standard h-type mesh refinement in which the error diminishes linearly with the logarithm of the number of elements [2] .

For the examinations of error associated with the grain size distributions, boundary representations and features of the microstructure, presented in the following sections, only two of the five discretizations were utilized—the 50K and 500K levels. These levels are noted at appropriate points in the discussion.

Influence of Grain Geometry

The influence of grain geometry on the errors associated with stress distributions was examined in terms of four types of grain geometries, as defined in "Virtual Samples: Instantiation and Loading" section and shown in Fig. 1: Voronoi, equiaxed, bimodal and grain growth tessellations. Recall that these tessellations exhibit qualitative differences in the
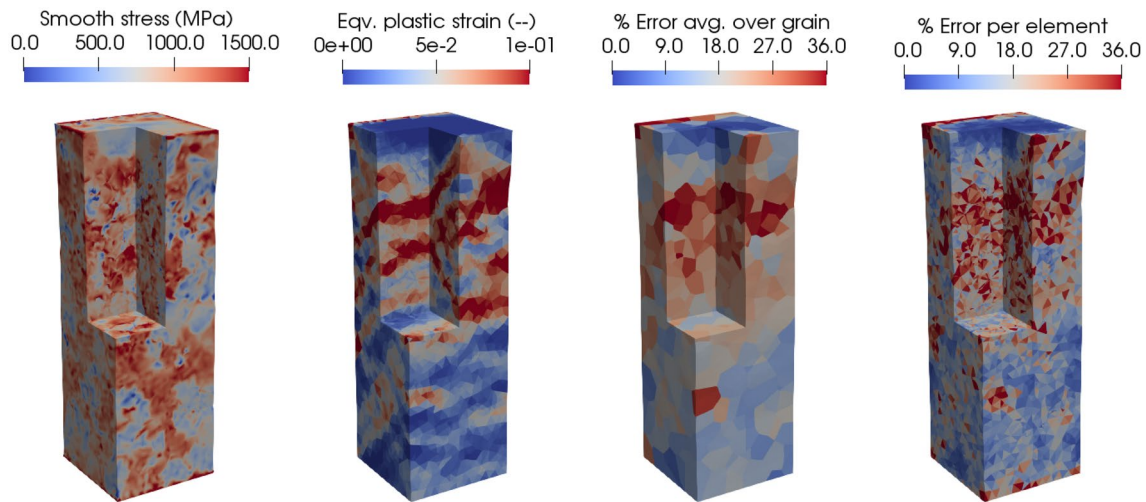
Fig. 8 The distributions of axial stress, equivalent plastic strain and errors in stress distribution over individual grains and over individual elements at 4.6% applied strain for the Voronoi sample with the dual texture. The small cut-out in the geometry shows the behavior inside the sample. The results are for the mesh with 50K elements

grain size and shape distributions, as quantified by the grain diameter and sphericity metrics in Fig. 2. The grain diameter distributions range from a narrow unimodal distribution for the equiaxed tessellation to the distribution with widely separated peaks for the bimodal tessellation. Between these lie the Voronoi and grain growth tessellations. The sphericity distributions differ primarily in the widths of the distributions, with the Voronoi tessellation exhibiting the broadest range in shape.

All of the tessellations have 1000 grains and are deformed in uniaxial tension to ≈ 5% strain as summarized in "Virtual Samples: Instantiation and Loading" section using the mechanical properties for the α-phase of Ti–6Al–4V. Two levels of finite element discretization are reported here: 50K and 500K elements. The stress distributions were computed for all combinations of the tessellations and the discretizations over the full loading history. Using the methodology reported in "Error Estimation Methodology" section, smoothed stress distributions were computed and used to construct the error estimates. Figure 8 shows the error distributions for the baseline case (Voronoi tessellation and dual texture) at the end of the loading along with the distribution of effective plastic strain. Banding of the deformation is a prominent feature of the behavior, as is evident from the plot of effective plastic strain. Banding depends on the initial texture and correlates with lattice misorientations, as discussed in greater detail in "Correlation with Microstructural Features" section.

The evolution of the error estimate metrics is shown in Fig. 9 for the grain-averaged errors, E^g. Error values remain low within the elastic domain, but grow steadily as plastic strain accumulates. Increasing the mesh refinement

delivers a reduction in the error overall. The mean values of the error distributions are not highly sensitive to the type of tessellation, although the two tessellations with greater range of grain size (bimodal and grain growth) generate slightly larger mean values than the other two. Much more notable are the differences in the standard deviation histories. Tessellations with larger grain size variations display larger standard deviations in the error distributions. The standard deviation for the bimodal tessellation is markedly higher, by approximately a factor of two, than the standard deviation of the equiaxed tessellation.

The error metrics indicate that grain size and shape have significant influences on predicted stress field and the allied error values. Within the limited number of tessellations examined, grain size variations have a stronger effect on errors in comparison with grain shape variations. Comparing the grain growth tessellation to the Voronoi tessellation illustrates this point. For both tessellations, the grains are more or less spherical in shape, but the grain growth tessellations generate higher errors. The grain growth tessellation has a large variety of grain sizes wherein small and large grains are often located next to each other. The bimodal tessellation has characteristics of both size and shape variations, although the size difference is the dominating parameter for this sample. This case develops larger error variations compared to any other tessellation. In contrast, the uniformity of size present in the equiaxed tessellation offers the most favorable situation for stress prediction. It is important to note that the larger grains contain more elements than smaller grains in the same geometry and that might influence the
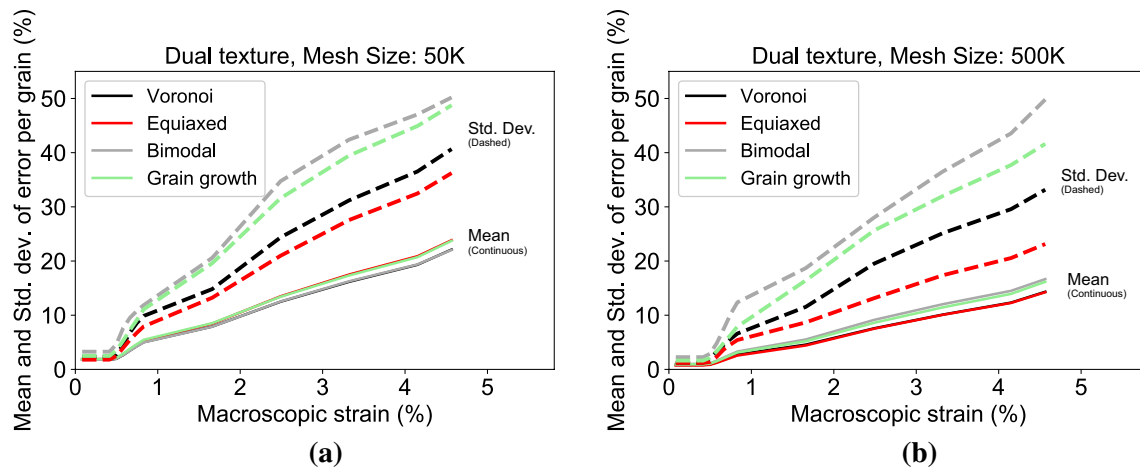
Fig. 9 Evolution of the mean and standard deviation of the grain-level error values with applied strain for the four different types of microstructure: Voronoi, equiaxed, bimodal and grain growth using the dual texture and two levels of discretizations (50K and 500K elements)
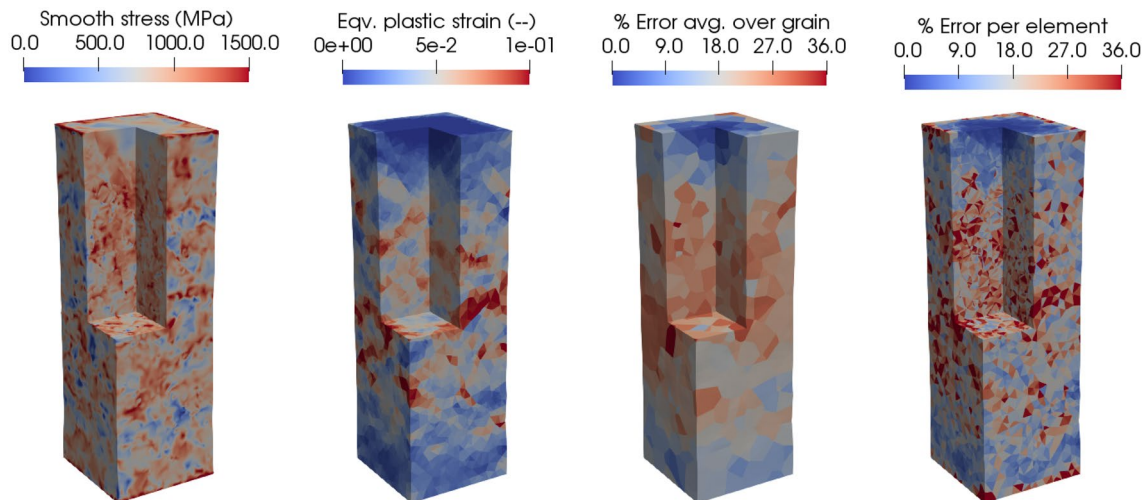

Fig. 10 The distributions of axial stress, equivalent plastic strain and errors in stress distribution over individual grains and over individual elements at 4.6% applied strain for the Voronoi sample with the uniform texture. The small cut-out in the geometry shows the behavior inside the sample. The results are for the mesh with 50K elements

grain-averaged error distribution over the geometry in the current study. Using local mesh refinements for small grains to generate uniform grain-averaged error distributions provides a good scope for future improvements on the current work.

Influence of Initial Texture

The simulations were repeated for the four types of microstructures using the uniform texture in place of the dual texture. Distributions of stress, deformation and error for the Voronoi tessellation with the uniform texture

are shown in Fig. 10 and can be contrasted with Fig. 8. The crystallographic texture has a strong influence on the error distributions through its influence of the heterogeneity of the deformation. The strong deformation band exhibited in the corresponding sample with the dual texture is no longer presented, and correspondingly, the spatial distribution of error is more diffuse. Correlations between the deformation and the error are discussed in "Correlation with Microstructural Features" section.

The error distribution metrics for the uniform texture simulations (Fig. 11) also provide evidence of the influence of the texture on errors in the stress predictions.
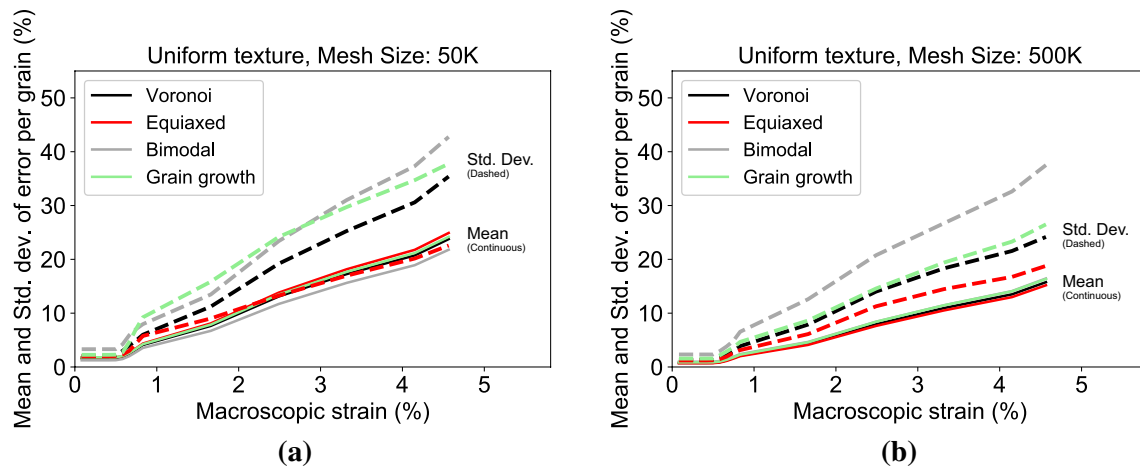
Fig. 11 Evolution of the mean and standard deviation of the grain-level error values with applied strain for the four different types of microstructure: Voronoi, equiaxed, bimodal and grain growth using the uniform texture and two levels of discretizations (50K and 500K elements)

Overall, the mean values are comparable between the two textures, but the standard deviations differ significantly.

Influence of Grain Boundary Representation

Tessellation methods differ significantly in how the grain boundaries are represented as a consequence of how the grain domains are defined. For Voronoi tessellations, the domain is defined by an inner envelope of intersecting planes. The planes are created from the bisections of space equidistance between any two seed points of the tessellation. In contrast, a rasterized tessellation creates a grain from the union of voxels spatially proximate to its seed point. Such tessellations are readily generated from voxel-based characterization methods (like EBSD or X-ray diffraction). For the same seed points, these two different methods can produce microstructures with very similar grain arrangements. However, one will have smooth grain boundaries and the other serrated grain boundaries unless further processing is done to the geometric input such as the methods described in [20]. It is expected that these differences in grain definitions would influence computed stress distributions and thus potentially influence the accuracy of the stress predictions.

Two possibilities emerge that bear on the stress distributions and their accuracy. First, because the computational domains are indeed different, the solutions, in general, will be different. In spite of the domains being distinct, the solutions nevertheless should bear strong similarities, as both are attempting to model essentially the same real microstructure. Second, the distinct computational domains each will have their own convergence characteristics as the converged solutions will be distinct as well. Here, the latter possibility is examined via the error estimation methodology discussed in

this paper. In particular, the distributions of error are examined for samples having the same numbers of grains, each with the same initial tessellation.

From the set of four microstructures defined in "Virtual Samples: Instantiation and Loading" section, two, the equiaxed and the bimodal, were chosen for examination relative to the grain boundary representation. These two generated the least and greatest standard deviations of error, respectively, for the baseline case as discussed in "Influence of Grain Geometry". The smooth grain boundary and serrated grain boundary samples have the same grain seed points for each of the two types of microstructures. However, the different instantiation approaches define different grain domains, one with smooth and the other with serrated grain boundaries. The initial lattice orientations for the grains are the same for each type of microstructure and were drawn from the dual texture. Simulations were performed using the Ti–6Al–4V single-crystal properties given in "Virtual Samples: Instantiation and Loading" section and the more refined discretizations having 500K elements. The error distributions are displayed for the equiaxed grain distribution in Fig. 12 (distributions for the bimodal microstructure show similar trends at the conclusion of the loading). Visual examination of the average grain errors suggests that the serrated grain boundary sample have higher error levels in corresponding grains in comparison with smooth grain boundary sample.

To be more precise about the influence of the grain boundary representation, it is useful to compare the metrics of the error distributions, which are provided in Fig. 13. The metrics reveal interesting differences between the two types of microstructures (equiaxed and bimodal) in regard to the influence of the boundary representations (smooth and serrated). For the equiaxed samples, the
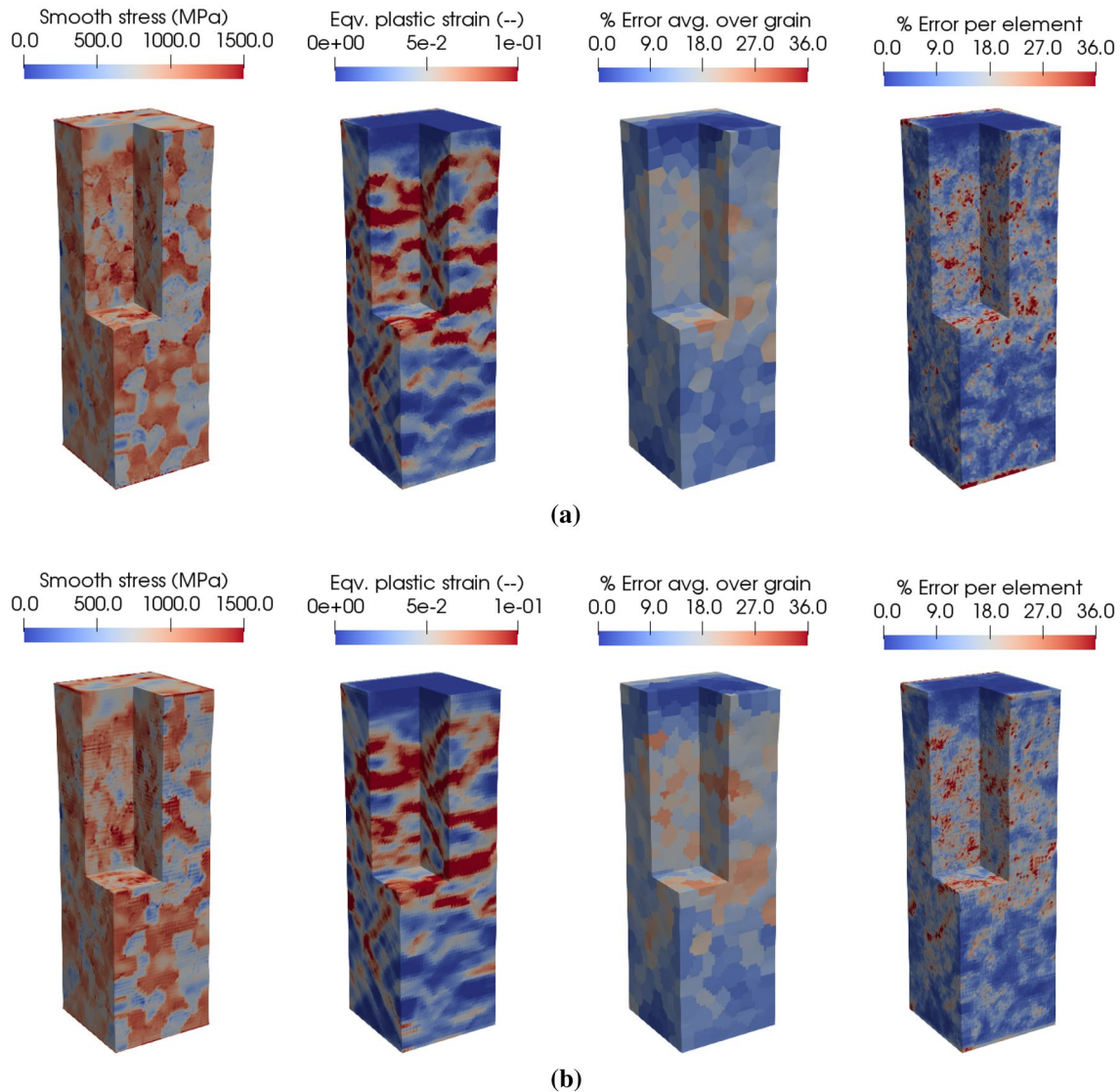
(a)

(b)

Fig. 12 The geometry showing the distribution of axial stress, equivalent plastic strain, percentage error in stress distribution over individual grains and over individual elements at 4.6% applied strain for the equiaxed samples with **a** smooth grain boundaries and **b** serrated or rough grain boundaries. The small cut-out in the geometry shows the behavior inside the sample. The results are for the mesh with 500K elements

samples with serrated grain boundaries displayed modestly higher values for both the mean and standard deviation of the error distributions. The differences were consistent throughout the loading history. In contrast, for the bimodal samples, the samples error distribution metrics changed their relative orders as the deformation proceeded. A crossover point occurred between 2 and 3% strain. While it cannot be concluded definitively, a cause of this may be a transition from the error highest around grain boundaries to it being highest in the grain interiors due to the large strain gradients associated with the plastic strain bands. If this is correct, then whether there is a crossover point and, if so, at what strain it occurs is likely to be sample

dependent. Correlation of the deformation heterogeneity to the error is discussed in greater detail in "Correlation with Microstructural Features" section.

Correlation with Microstructural Features

Using the simulation results, it is possible to test for the existence of correlations between microstructural features and error in the computed stress distributions. This has been done for all four types of microstructures (Voronoi, equiaxed, bimodal and grain growth) with each of the two initial textures (uniform and dual). The results presented were generated using 1000 grain samples discretized with 500K
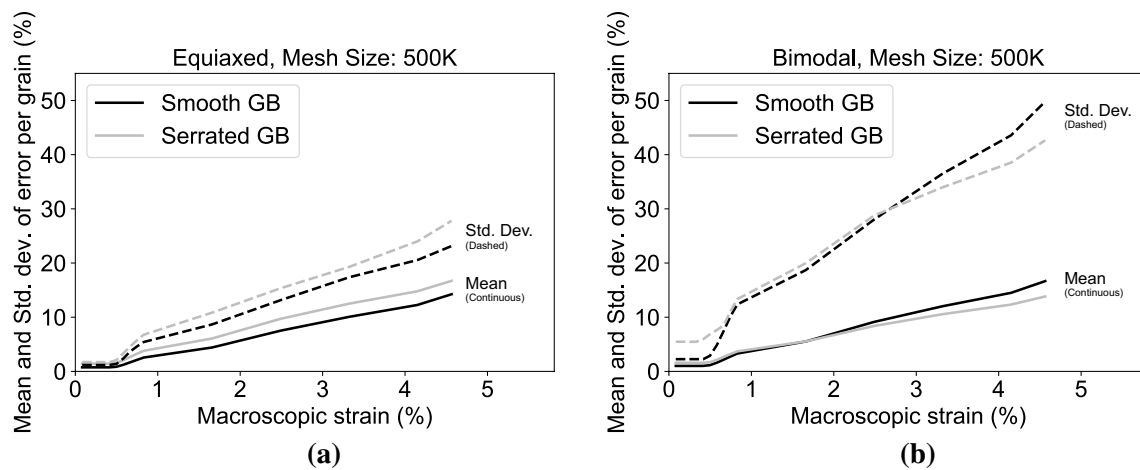
Fig. 13 Evolution of the mean and standard deviation of the grain-level error values with applied strain for the smooth and serrated grain boundary samples using dual texture and mesh with 500K elements for **a** equiaxed samples and **b** bimodal samples shown in Figs. 1 and 4, respectively
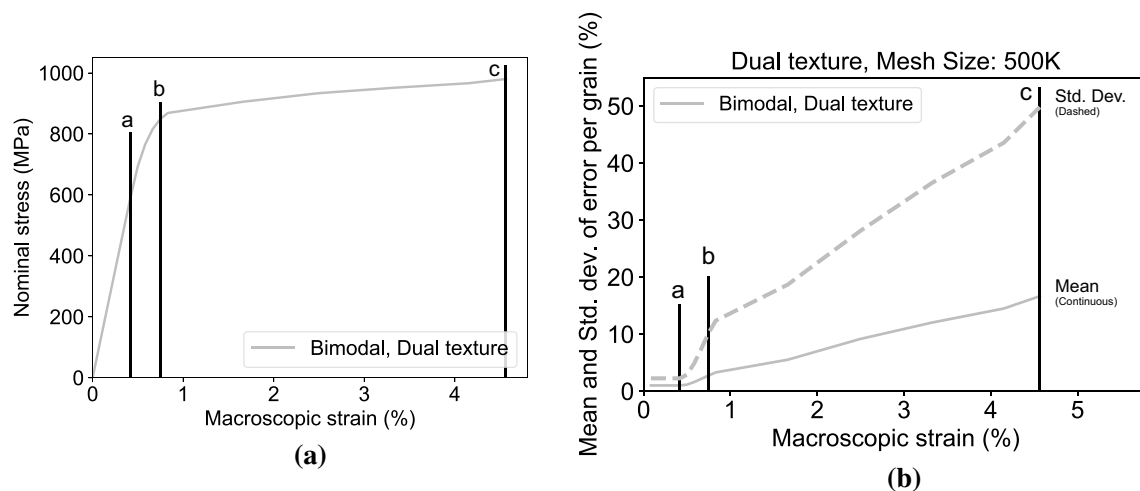

Fig. 14 **a** Stress–strain response with markers for contour plots shown in Fig. 15; **b** Error metric histories with markers for contour plots shown in Fig. 15. Point (a) is in the elastic regime, Point (b) is in the elastic–plastic transition, and Point (c) is in the fully developed plasticity regime

elements and subjected to tensile loading. All cases exhibit similar trends to that discussed in previous sections of the paper. Consequently, we focus our discussion here primarily on just one of the eight cases (bimodal microstructure with dual texture). Statistics are presented, however, for all eight cases. Additional contour plots for several other cases are provided in the supplement entitled, "Supplemental Results".

The spatial distribution of error evolves qualitatively, as well as quantitatively, over the course of the deformation history. This is because the character of the deformation changes over the history, proceeding from the initial elastic regime into the elastic–plastic transition and finally operating in the fully developed plastic regime as the sample is deformed to an average strain of ≈ 5%. As the loading

progresses through these regimes, the stress state evolves in concert with the evolving heterogeneous deformation patterns. To illustrate the correlation between the error distributions and the regime of deformation, three sets of contour plots are presented and discussed. Figure 14 shows the macroscopic stress–strain response for the sample and the corresponding histories of the metrics of the error distributions. Three points are indicated on the plots (Points (a), (b) and (c)), which correspond to strains at which contour plots are shown in Fig. 15. Point (a) is in the elastic regime, Point (b) is in the elastic–plastic transition and Point (c) is in the fully developed plasticity regime.

Five contour plots are provided in Fig. 15 for each level of strain. Shown, from left to right, are: the grains, delineated by the current lattice orientation; the effective plastic
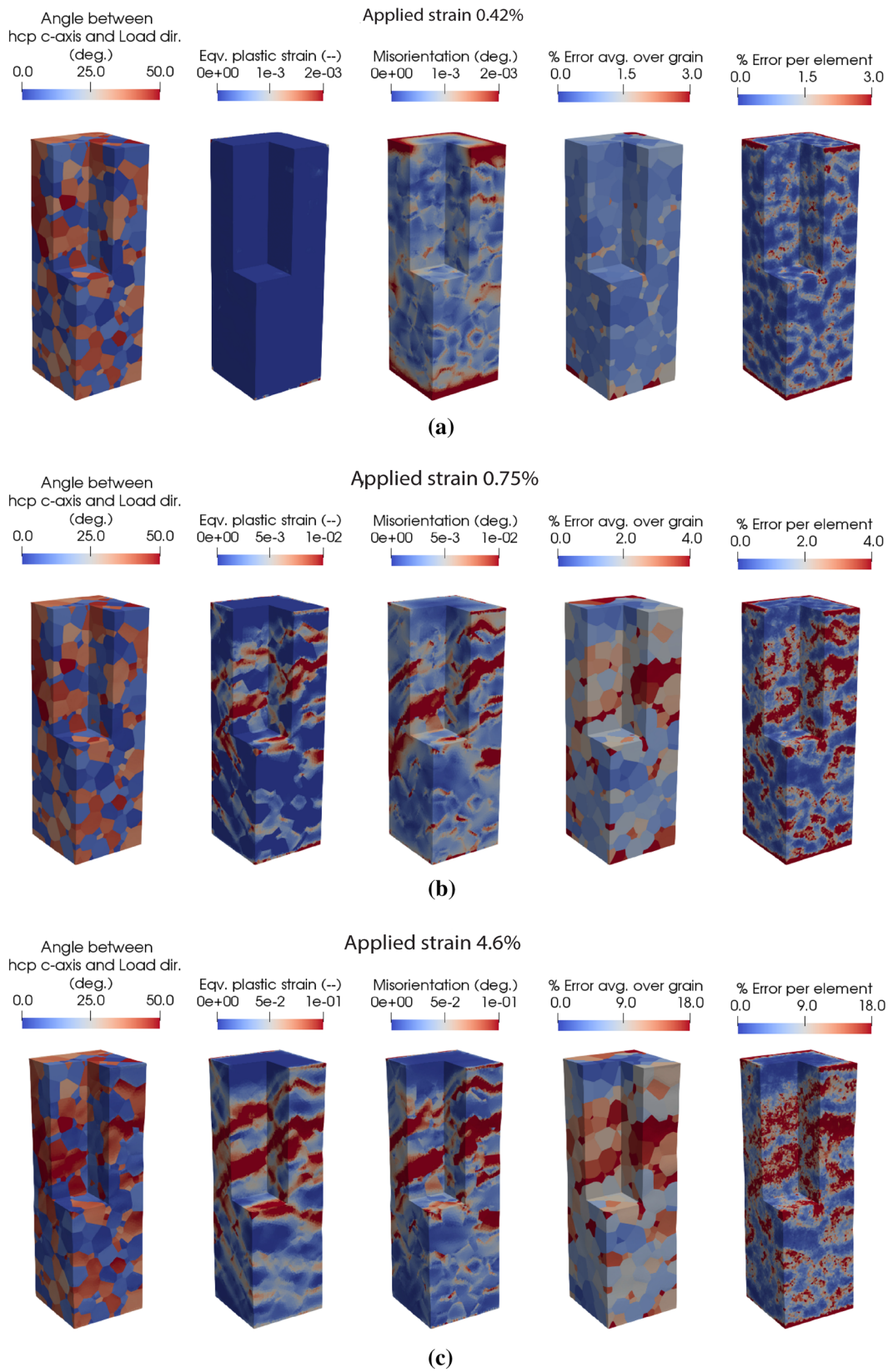
Fig. 15 Bimodal microstructure with dual texture; tensile loading. Left to right: grain orientation; plastic strain; misorientation; grain error; element error. Distribution shown for applied strain of **a** 0.42% (elastic regime), **b** 0.7% (macroscale elastic–plastic transition) and **c** 4.6% (plastic regime)

strain; the lattice misorientation (referenced from the initial grain orientations); the grain-averaged stress error; the elemental stress error. The lattice misorientation is calculated between the initial (q_i) and current (q_c) orientations of an element and is expressed in terms of quaternions:

$$\Delta q = q_i^{-1} \, q_c \tag{8}$$

The misorientation angle, $\Delta\theta$, is given by:

$$\Delta\theta = 2 \cos \Delta q_0 \tag{9}$$

where Δq_0 is the scalar component of the misorientation quaternion Δq. $\Delta\theta$ is plotted here to illuminate the correlations between distributions of misorientation and error of the stress. Comparing the corresponding images at increasing levels of strain, evolution is evident in all of the fields plotted. Plastic strains develop, eventually forming clearly resolved bands; lattice orientations rotate with slip, exhibiting intragrain misorientations due to deformation heterogeneity within grains, and errors in the stress strengthen in magnitude as the deformation increases. The lattice misorientation develops most strongly in highly deformed regions where the errors also grow larger with increasing strain.

In the elastic regime (Fig. 15a), there is virtually no plastic strain[1] and lattice misorientation is minimal (note the scale). Nevertheless, the error is present before the onset of plastic flow. Error in the stress distribution is expected at all levels of stress unless the computed stress matches the exact, which is typically not possible at finite levels of resolution. The magnitude of the error correlates with proximity to the grain boundaries. Prior to loading the sample, the lattice orientation is initially uniform within grains. It remains nearly uniform throughout the elastic regime because the strains and rotations are small everywhere. As long as the sample remains elastic, the largest gradients of the deformation field tend to occur near the grain boundaries. Without enhancing the spatial resolution of the mesh in the vicinity of the grain boundaries, the errors tend to be larger near the grain perimeter and smaller in the grain interior. The mean error levels remain relatively low throughout the elastic regime—approximately 1%, as indicated in Fig. 14b. Recognizing that stress gradients tend to be higher near grain boundaries than in the grain interior, Resk and colleagues [21] based an a priori mesh refinement strategy (both for the initial meshing and for re-meshing) on the proximity of an element to a grain boundary. They demonstrated that using higher element densities near the grain boundaries provided more effective allocation of the elements and reduced errors in comparison with non-adaptive meshing.

Plastic deformation initiates before the sample reaches 1% strain, as is apparent from the stress–strain response shown in Fig. 14a and the plastic strain distribution shown in Fig. 15b. The plastic deformation is spatially heterogeneous: the bands that appear at 0.7% sample strain are well-formed by 4% sample strain (Fig. 15c). Lattice rotation accompanies plastic flow by slip, leading to intragrain lattice misorientations in grains with heterogeneous deformation fields. From the misorientation distributions shown in Fig. 15c, it is evident that misorientation is high in the deformation bands. From the perspective of the errors in the stress distributions, a major transition in the spatial position of regions of high error occurs during the elastic–plastic transition. Domains of highest error shift from the grain boundaries to the deformation bands. Error levels constantly grow in concert with the misorientation levels as the plastic deformation increases, as indicated by the evolution of the error distribution metrics given in Fig. 14b.

To quantify a correlation between the error and misorientation or plastic deformation, the Spearman correlation was used [22]. The Spearman correlation is a nonparametric measure of how the relationship between two variables can be described by a monotonic function [23, 24], whether linear or nonlinear. This coefficient was generated for each test case at 0.4%, 0.7% and 4.6% strain. The Spearman correlations for the different cases are summarized in Table 4. It was found that plastic deformation and misorientation are not correlated with the error at 0.4% and 0.7% strain. However, once the samples reached 4.6% strain, the plastic deformation and misorientation were shown to have a moderate, positive correlation with the error, with all values of the Spearman coefficient ranging between 0.4 and 0.7. Across all of the test cases at 4.6% strain, the plastic deformation had a stronger correlation when compared to the misorientation. Another observation made from these correlations was that the dual texture cases resulted in a stronger correlation when compared to the uniform texture cases. Further tests would need to be conducted to see whether these correlations become stronger the further out the sample is strained.

The elemental error estimates are shown in Fig. 16 as correlations against the local plastic strain and the lattice misorientation at 4.6% macroscopic strain. These plots are for one point on the macroscopic stress–strain curve (Point (c) in Fig. 14) and show spatial heterogeneity of error that is associated with the spatial variability of strain and misorientation. This is in contrast to the growth of error with macroscopic strain over the entire loading history previously shown in Fig. 14b. To construct these plots, the elemental error values were sorted into 500 bins of either the (a) plastic strain or (b) the lattice misorientation. Error values within bins were averaged and plotted against the bin midpoint

---

[1] Rate-dependent crystal plasticity admits plastic flow at any resolved shear stress, but with low rate sensitivity the slip system activity is very small unless the resolved shear stress is close to the slip system strength.

Table 4 The tabulated results of the Spearman rank correlation coefficient for error versus either misorientation or plastic deformation across the different tessellations, textures and three macroscopic strain cases

Tessellation	Texture	Strain (%)	Misorientation correlation	Plastic deformation correlation
Bimodal	Dual	0.42	0.23	0.01
		0.75	0.40	0.41
		4.6	0.55	0.65
	Uniform	0.42	0.28	− 0.01
		0.75	0.31	0.29
		4.6	0.45	0.52
Voronoi	Dual	0.42	0.21	0.02
		0.75	0.44	0.49
		4.6	0.57	0.66
	Uniform	0.42	0.21	0.03
		0.75	0.33	0.39
		4.6	0.47	0.58
Grain growth	Dual	0.42	0.24	0.04
		0.75	0.44	0.54
		4.6	0.63	0.73
	Uniform	0.42	0.26	0.04
		0.75	0.36	0.35
		4.6	0.43	0.51
Equiaxed	Dual	0.42	0.19	0.01
		0.75	0.44	0.52
		4.6	0.58	0.68
	Uniform	0.42	0.24	0.03
		0.75	0.31	0.39
		4.6	0.51	0.61

value. For both plots, two trends are evident. First, the correlation shows less spread at lower values of plastic strain and lattice misorientations. At higher levels of strain and misorientation, the correlated behavior observed for low strain becomes increasingly noisy. Second, the errors for the coarser mesh are larger than for the finer mesh for the same level of plastic strain or lattice misorientation. This indicates that increased mesh resolution facilitates better estimation of stress in regions of high gradients. Note that the ranges of strain and misorientation are larger for the finer mesh, which can be attributed to finer mesh resolution capturing sharper gradients of the deformation and consequently producing sharper gradients in the lattice orientation.

The higher correlation between the plastic strain and stress error than between the misorientation and stress error as quantified by the Spearman rank coefficient in Table 4 merits further consideration. Plastic deformations can potentially impact the simulation accuracy in several ways. Plastic deformations result both in a change of shape of the body and in changes to its mechanical state. The plastic strain is a measure of the former—shape changes of the constituent grains. The mechanical state is characterized in the present model with the lattice orientation, the slip system strengths and the elastic strain. Plastic deformations alter the first two of these—the lattice orientations and the slip system strengths. The question arises: does the plastic strain exhibit a stronger correlation with error than misorientations because it increases concurrently with mechanical state evolution as well as shape changes or because the shape changes themselves are a principal source of higher levels of error? To answer this question, we consider the element quality based on the geometric metrics [25]. Elements in the
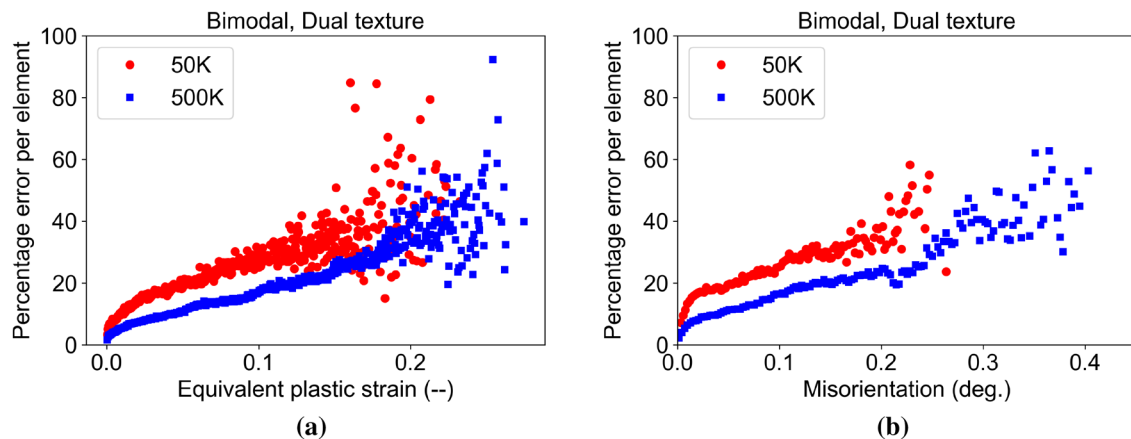

Fig. 16 Elemental error estimates at 4.6% macroscopic strain for the case of bimodal tessellation and dual texture. Error estimates shown for 50K and 500K element meshes. Errors are shown versus elemental **a** plastic strain and **b** lattice misorientation. Each point corresponds to the average error value within 500 bins for each distribution

mesh initially have acceptable quality owing to constraints imposed in mesh generation algorithms used by *Neper*. However, the shape changes associated with the plastic deformation can be detrimental to accuracy if the elements become too highly distorted. This effect can be quantified through changes in the Jacobians of the elemental parametric mapping. In *FEpX*, the coordinates are advanced during each time step using the converged velocity field. This will distort the elements and degrade the element quality if the Jacobian values over the element volume become fall outside acceptable limits [26]. If the elements are repaired at each timestep by returning the midside nodes of the tetrahedral elements to the center of the corresponding edge (as is done in *FEpX*), then the Jacobian remains constant over the element. Consequently, element degradation from distortion is not a source of the growing error in the stress distributions. We surmise instead that the stronger correlation between the stress error and the plastic strain is because gradients in the other state variables (slip system strength and elastic strain) also are captured to some extent with the plastic strain correlation.

Discussion

In this section, we discuss how the error in the computed stress distributions presented in the previous sections might impact future investigations that include simulations of mechanical behaviors of polycrystals. First, several important points are reiterated.

- Error accompanies heterogeneity in the stress, which follows from heterogeneity of the microstructure.
- At small strains, heterogeneity coincides with features in the initial microstructure, such as grain boundaries, irregular grain shapes or non-uniform distributions of grain size.
- At larger strains, additional heterogeneity in microstructure arises from gradients of the deformation—an example demonstrated here being intragrain lattice misorientations.
- In the examples examined here, the overall level of error grew substantially as plastic deformation accumulated spatially in bands and lattice misorientation concurrently increased.
- Efforts to mitigate the error by increasing the mesh resolution improved the stress prediction by reducing both the mean and standard deviation of the error distribution.
- Differences in grain shape and in the grain size distribution tended to influence the standard deviations of the error distributions more so than the means of the distributions.

- Samples with smooth, versus those with serrated, grain boundaries did not show unequivocal trends in terms of the error, as other factors (such as modality of the grain size or existence of strong texture) tended to dominate the error.

Error estimation is strongly suggested for investigations in which the determination of stress distributions is a primary objective. A baseline case can be examined critically with meshes of increasing refinement to check for convergence of critical quantities. Steps can be taken to assess the error in stress and to take remedial steps if required. We note two points in this regard. First, the impact of the error will be more severe if intragrain stress predictions are needed and less severe if average stresses, such as macroscopic or fiber-averaged values, are the end goal. Second, if the estimation of representative properties is a goal, the type of property being estimated sets constraints on the sample size. For example, estimating strength imposed different constraints on the size of a representative volume than does estimating stiffness [12]. These can influence the priorities set in controlling the metrics of the error distribution.

For studies focused on accuracy of the intragrain stress predictions, a few considerations are offered. At small strains (within the elastic domain), the process is relatively straightforward. The samples can be instantiated to control the grain size and shape metrics to produce tessellations with good fidelity [27]. Tessellation methods that provide equiaxed grains (uniform size and high sphericity) give lower errors than other tessellations. If no experimental information is available regarding grain size and shape distributions, the equiaxed tessellations are preferred for limiting errors in the stress distribution. It is probably advisable to maintain smooth grain boundaries to the extent possible. Further, steps can be taken to guarantee a high-quality mesh is built based on the geometry of the microstructure, as discussed and demonstrated in [28]. At larger strains, however, the process becomes more complicated. Deformation-induced heterogeneity controls the growth of error over the course of the loading. Adaptive mesh refinement should be considered in applications that exhibit significant strain localization. In this case, adaptive re-meshing is a more certain approach to high confidence than simple mesh refinement.

Conclusions

An established methodology for estimating errors of the stress distribution has been implemented for simulations of polycrystals. The methodology operates on the premise that the stress distribution will be a continuous function over grains wherein the lattice orientations are also continuous fields.

The following observations can be drawn from the estimated error distributions presented in this paper:

1. Stress uncertainty reduces with increased mesh resolution in terms of both the mean and standard deviation values of the stress distributions.
2. Mean values of the stress distributions are not as strongly dependent on the grain size distributions as are the standard deviations.
3. Stress errors are moderately higher in samples with serrated (voxel) grain boundaries compared with smooth grain boundaries.
4. Estimated errors of the stress distributions are low at small strains, where the intragrain lattice orientation is nearly uniform and the response is elastic; larger errors correlate with proximity to the grain boundaries.
5. Estimated errors of the stress distributions are much higher at strains in the fully developed plastic regime; larger errors correlate with deformation bands where lattice misorientations are high.
6. Overall, structural factors that promote deformation heterogeneity can have a substantial impact on stress uncertainty. This is apparent from the differences between the uniform and dual texture results.

Based on the results presented here, several possibilities are apparent for improving stress predictions in polycrystal, elastoplastic simulations. These range from relatively straightforward post-processing of stress distributions of the current models to much more involved extensions of the current methodologies. Here are a number of these:

1. No effort has been made here to determine the optimal method for computing error. Given the importance of assessing error in the stress in general and the trends reported herein regarding modeling variables, an effort targeted at determining the optimal method has a substantial merit.
2. Methods to improve the accuracy of the computed stress could be put to effective use, including stress recovery, error-based mesh refinement and adaptive re-meshing.

   - *Stress recovery* utilizes a posteriori local and global methods, especially for stress fluctuations in vicinity of grain boundaries. This could be done with stress distributions of particular importance to the analyst, such as those being used in direct comparisons to experimental data.
   - *Error-based mesh refinement* is the most useful for improving solutions at a particular state of deformation. As noted previously, the locations of high error change as the deformation proceeds, so error-based

refinement might be necessary for solutions at critical points in the loading.
   - *Adaptive re-meshing* the results point highest errors develop in zones of more intense deformation. The spatial location of the deformation bands is not known a priori, so the polycrystal could be adaptively re-meshed to increase element densities in large deformation zones and decrease element densities elsewhere. This could improve the stress accuracy more economically than simply refining the uniformly over the polycrystal.

3. Intragrain lattice continuity was not explicitly enforced in the simulations reported here, but may offer a pathway to lower errors in the stress distributions in more highly deformed samples. Recent work done in [29] provides the necessary framework in order to verify this premise.

In closing, the results presented in this paper explore the influences of several modeling factors on the accuracy of finite element stress distributions in deforming polycrystals using an existing methodology to estimate the error levels in the stress. Mesh refinement reduces error consistent with previously reported trends for h-type discretization. The spatial locations of higher error shift from grain boundaries to zones of high lattice misorientation as the sample loading proceeds from the elastic regime through the elastic–plastic transition and into fully developed plastic flow. The results point to additional steps that can be taken to further improve stress predictions.

Compliance with ethical standards

Conflict of interest On behalf of all authors, the corresponding author states that there is no conflict of interest.

References

1. Roters F, Eisenlohr P, Hantcherli L, Tjahjanto DD, Bieler TR, Raabe D (2010) Overview of constitutive laws, kinematics, homogenization and multiscale methods in crystal plasticity finite-element modeling: theory, experiments, applications. Acta Mater 58(4):1152–1211
2. Zienkiewicz OC, Taylor RL, Zhu JZ (2005) Chapter 13. The finite element method its basis and fundamentals, 6th edn. Elsevier Butterworth-Heinemann, Amsterdam

3. Oden JT, Moser R, Ghattas O (2010) Computer predictions with quantified uncertainty, part 1. SIAM News 43(9):1–3
4. Oden JT, Moser R, Ghattas O (2010) Computer predictions with quantified uncertainty, part 2. SIAM News 43(10):1–4
5. Buchheit TE, Wellman GW, Battaile CC (2005) Investigating the limits of polycrystal plasticity modeling. Int J Plast 21:221–249
6. Poshadel AC, Gharghouri M, Dawson PR (2019) Sensitivity of crystal stress distributions to the definition of virtual two-phase microstructures. Metall Mater Trans A. https://doi.org/10.1007/s11661-018-5085-2
7. Rizzi R, Jones RE, Templeton JA, Ostien JT, Boyce BL (2017) Plasticity models of material variability based on uncertainty quantification techniques. arXiv:1802.01487v1 [cond-mat.mtrl-sci]
8. Zienkiewicz Olgierd C, Zhu Jian Z (1987) A simple error estimator and adaptive procedure for practical engineering analysis. Int J Numer Methods Eng 24(2):337–357
9. Dawson PR, Boyce DE (April 2015) FEpX—finite element polycrystals: theory, finite element formulation, numerical implementation and illustrative examples. ArXiv e-prints
10. Kasemer M, Quey R, Dawson P (2017) The influence of mechanical constraints introduced by β annealed microstructures on the yield strength and ductility of Ti–6Al–4V. J Mech Phys Solids 103:179–198
11. Kasemer M, Echlin MP, Stinville JC, Pollock TM, Dawson P (2017) On slip initiation in equiaxed α/β Ti–6Al–4V. Acta Mater 136:288–302
12. Chatterjee K, Echlin MP, Kasemer MP, Callahan PG, Pollock TM, Dawson PR (2018) Prediction of tensile stiffness and strength of Ti–6Al–4V using instantiated volume elements and crystal plasticity. Acta Mater 157:21–32
13. Ainsworth M, Tinsley Oden J (1997) A posteriori error estimation in finite element analysis. Comput Methods Appl Mech Eng 142(1):1–88
14. Becker R, Rannacher R (2001) An optimal control approach to a posteriori error estimation in finite element methods. Acta Numer 10:1–102
15. Grätsch T, Bathe K-J (2005) A posteriori error estimation techniques in practical finite element analysis. Comput Struct 83(4):235–265
16. Lütjering G, Williams JC (2007) Titanium. Engineering materials and processes, 2nd edn. Springer, Berlin
17. Quey R, Dawson PR, Barbe F (2011) Large-scale 3D random polycrystals for the finite element method: generation, meshing and remeshing. Comput Method Appl Mech Eng 200(17):1729–1745
18. Wielewski E, Boyce DE, Park J-S, Miller MP, Dawson PR (2017) A methodology to determine the elastic moduli of crystals by matching experimental and simulated lattice strain pole figures using discrete harmonics. Acta Mater 126:469–480
19. Dawson PR, Boyce DE, Park J-S, Wielewski E, Miller MP (2018) Determining the strengths of HCP slip systems using harmonic analyses of lattice strain distributions. Acta Mater 144:92–106
20. Maddali S, Ta'asan S, Suter RM (2016) Topology-faithful non-parametric estimation and tracking of bulk interface networks. Comput Mater Sci 125:328–340
21. Resk H, Delannay L, Bernacki M, Coupez T, Log'e R (2009) Adaptive mesh refinement and automatic remeshing in crystal plasticity finite element simulations. Model Simul Mater Sci Eng 17:1–22
22. Spearman C (1904) The proof and measurement of association between two things. Am J Psychol 15(1):72–101
23. McDonald JH (2014) Handbook of biological statistics, 3rd edn. Sparky House Publishing, Baltimore, pp 209–212
24. Zwillinger D, Kokoska S (2000) CRC standard probability and statistics tables and formulae, chapter 14.7. Chapman & Hall, London
25. Skroch M, Owen SJ, Staten ML, Quadros RW, Hanks B, Clark B, Hensley T, Meyers RJ, Ernst C, Morris R, McBride C, Stimpson C (2019) Cubit geometry and mesh generation toolkit 15.4 user documentation. Sandia National Laboratories
26. Knupp PM (2000) Achieving finite element mesh quality via optimization of the Jacobian matrix norm and associated quantities, part I. Int J Numer Methods Eng 48(3):401–420
27. Quey R, Renversade L (2018) Optimal polyhedral description of 3D polycrystals: method and application to statistical and synchrotron X-ray diffraction data. Comput Methods Appl Mech Eng 330:308–333
28. Owen SJ, Brown JA, Ernst CD, Lim H, Long KN (2017) Hexahedral mesh generation for computational materials modeling. Procedia Eng 203:167–179
29. Carson R, Dawson P (2019) Formulation and characterization of a continuous crystal lattice orientation finite element method (LOFEM) and its application to dislocation fields. J Mech Phys Solids 126:1–19
30. Ahrens J, Geveci B, Law C, Hansen C, Johnson C (2005) ParaView: an end-user tool for large-data visualization. In: Hansen CD, Johnson CR (eds) The visualization handbook, vol 717. Elsevier, Amsterdam, pp 717–731